J Mater Sci: Mater Electron (2021) 32:19042–19051

Effect of 6 MeV electron irradiation on nano-Cu_2ZnSnS_4

S. P. Kandare[1], V. N. Bhoraskar[1], A. B. Phatangare[1], Rekha Rao[2,3], Mala N. Rao[2,3,*], S. D. Dhole[1], and S. S. Dahiwale[1,*]

[1] *Microtron Accelerator Laboratory, Department of Physics, Savitribai Phule Pune University, Pune 411007, India*
[2] *Solid State Physics Division, Bhabha Atomic Research Centre, Mumbai 400085, India*
[3] *Homi Bhabha National Institute, Mumbai 400094, India*

Received: 1 February 2021
Accepted: 15 June 2021
Published online: 9 July 2021

ABSTRACT

Microwave synthesized nano-sized Cu_2ZnSnS_4 (CZTS) powder was irradiated with 6 MeV electrons, to investigate stability under radiation. The structural, optical, vibrational and morphological properties were explored using X-ray diffraction, UV–Visible spectroscopy, Raman spectroscopy and scanning electron microscope (SEM). The irradiated sample shows significant change in properties when compared with the pristine sample. X-ray peak broadening analysis has been used to estimate the crystallite size and lattice strain. Raman spectroscopy analysis confirms the transition of ordered kesteriteto disordered kesterite phase after electron irradiation at electron fluence of 4×10^{15} e^-/cm^2. CZTS nanoparticles having hierarchical flower-like morphology starts agglomerating after electron irradiation as observed from SEM images. The sample did not amorphize up to the highest fluence4×10^{15} e^-/cm^2employed in this study.

1 Introduction

All the spacecrafts and satellites use photovoltaic solar cell power in space as an energy source [1]. For many decades in conventional spacecrafts Si [2–5], multi junction solar cell [6–9] and GaAs/Ga are used [10–13] which provide high efficiency and are also quite robust to space environment. Researchers are trying to replace it with an alternate. Photovoltaic thin film solar cell array which offers high reliability, lower production cost, proven manufacturing and scalability of required power levels have been shown as useful for space mission [14]. The report from M. R. Reddy suggests that conventional solar cell can be replaceable with flexible thin film solar cell array of CIGS-based solar cell that reduces not only mass, but also lowers the cost by ~ 30% as compared to the conventional space solar cell [15].

One of the most important necessities of space solar cell is the ability to withstand harsh space radiation environment. The energetic particles in space environments such as proton, electron, gamma etc. cause lattice damage in an active area of solar cell which degrades the performance of the solar cell used as a power sources in space satellite [10–16]. This puts a limit on the use of solar cell for longer duration. Therefore, the stability of material which is used for making the solar cell for space application is very important. A study by Jaseneket al., shows that $CuInGaSe_2$ (CIGS) solar cell can tolerate more than 10

Address correspondence to E-mail: mala@barc.gov.in; ssd@physics.unipune.ac.in

https://doi.org/10.1007/s10854-021-06420-5

Table 1 Comparison of previous and present work on effects of irradiation on CZTS

	Souli et al. [19]	Sugiyama et al. [20]	Suvanam et al. [21]	Our work
Sample form	Thin films synthesized by spray pyrolysis technique, deposited on glass substrates	Solar cell	Solar cell	Nano-powder
Irradiation type	Gamma	2 MeV electrons, 380 keV protons	3 MeV protons	6 MeV electrons
Dose/fluence	10–100 kGy	10^{14}–2×10^{17} cm^{-2} for electrons, 10^{12}–3×10^{16} cm^{-2} for protons	10^{10}–10^{13} cm^{-2}	1–4 $\times$ 10^{15} cm^{-2}
Characterization methods	X-ray diffraction, spectrophotometer and scanning electron microscope	Photoluminescence (PL) measurements, current density–voltage (J–V) curves	Current density–voltage (J-V) curves, external quantum efficiency (EQE)	X-ray diffraction, UV–Visible spectroscopy, Raman spectroscopy and Scanning Electron Microscope
Results	Increase in crystallite size from 52 to 79 nm has been observed after irradiation with 100 kGy gamma dose, band gap energy have increased and reached 1.6 eV at 100 kGy gamma dose	Photoluminescence peak intensity decreased and electrical performance parameters V_{OC}, J_{SC} and η decrease with increasing irradiation fluence	For the highest dose, the saturation current I_o increased by 10 times, a decrease in the EQE can be observed in the higher-wavelength region	Phase transition from ordered kesterite to disordered kesterite for 4 $\times$ 10^{15} e^{-}/cm^2 irradiation fluence, decrease in crystallite size from 14.4 nm to 10.8 nm with increase in electron irradiation, bandgap of the material changed from 1.5 eV to 3.95 eV, morphology of hierarchical flower Cu_2ZnSnS_4 start agglomerating with electron irradiation
Conclusions	Structural properties of CZTS films have improved by gamma irradiation while the optical properties have slightly changed, which is favourable for optoelectronic applications working in nuclear environments	Normalized efficiency of solar cells decreased when fluence was greater than $\sim$ 10^{15} cm^{-2} for electron irradiation or 10^{12} cm^{-2} for proton irradiation	CZTS technology has superior radiation hardness	The samples did not amorphize in the fluence range used and thus indicate radiation stability

times larger fluence of high energy electrons than any other solar cell [17]. This study was further strengthened by Karsten Otte et al., which reported that flexible CIGS thin film solar cells are superior to that of GaAs with respect to radiation hardness [18]. However, indium and gallium are rare earth metals, due to which cost of solar cell is high. Therefore, the necessity of alternative material to CIGS is needed which can stand harsh radiation environment.

Very recently Souli et al., reported that after gamma irradiation the structural and optical properties of Cu_2ZnSnS_4 (abbreviated as CZTS hereafter) thin films improves, making them favourable in order to use them in outer space where gamma

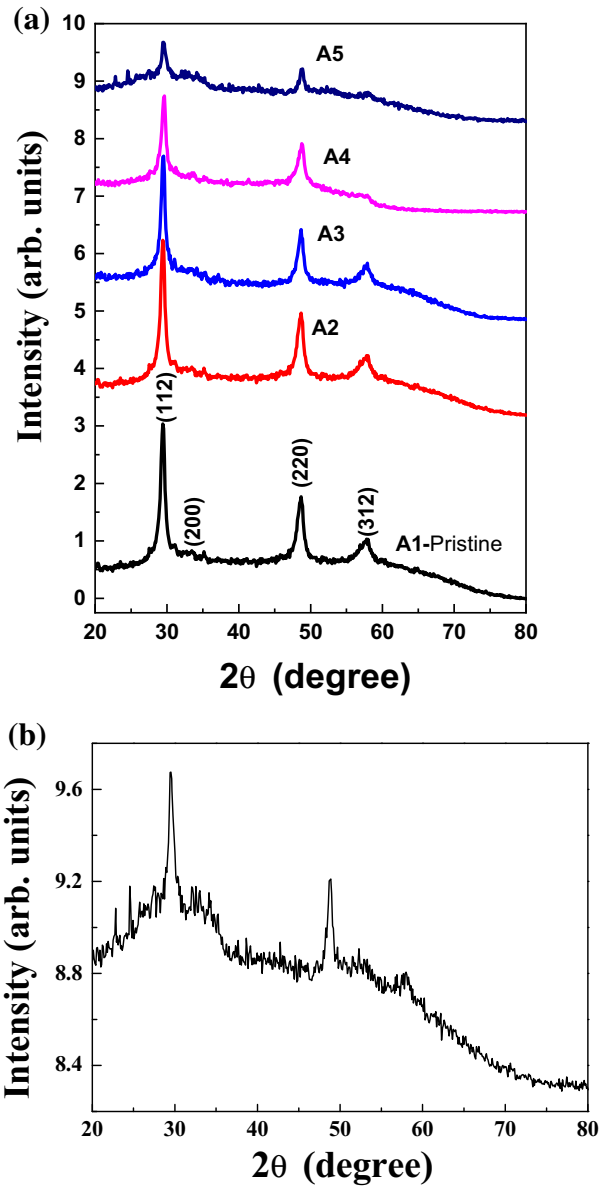

Fig. 1 **a** X-ray diffraction patterns of Cu_2ZnSnS_4 samples irradiated with 6 MeV electron at different irradiation fluences. **b** An expanded view of X-ray diffraction pattern of Cu_2ZnSnS_4 sample irradiated with 6 MeV electron at 4×10^{15} e^-/cm^2 irradiation fluence

radiation is abundant [19]. In another study, Sugiyama et al. reported effect of electron and proton irradiation on CZTS solar cell. In their study they reported the effect of electron irradiation using constant energy of 2 MeV and the fluence was varied from 1×10^{14} e^-/cm^2 to 2×10^{17} e^-/cm^2, while for proton irradiation, the energy was kept 380 keV from a 400 kV ion implanter with fluence ranging from 1×10^{12} to 3×10^{16} cm^{-2}. They claimed CZTS solar cell performance improves up to small amount for both electron and proton irradiations, which shows that CZTS solar cell tolerates electron and proton irradiation analogous to CIGS solar cell [20]. Similar study was also done by Suvanam et al., where thin films of Cu_2ZnSnS_4/Se_4 (CZTSSe) and CZTS were investigated after 3 MeV proton irradiation; it showed that CZTSSe and CZTS are high-radiation hardened materials as compared to CIGS solar cell [21]. In continuation with these studies, we have carried out an experimental study in which our objective was to explore the effect of 6 MeV electron irradiation on CZTS nanoflower-like structures. Further we carried out detailed analysis using micro-Raman spectroscopy to investigate how the structure changes or modifies upon irradiation. There are no reports available on structural transition of CZTS due to electron irradiation. Earlier Parkin et al. reported, how the presence of electron beam induces sulphur vacancies in monolayer of $MoS_2$and Raman spectroscopy was used as non-destructive method to estimate defect concentration in MoS_2 [22].

In our study, we report 6 MeV electron irradiation induced changes on nanocrystalline CZTS (size ~ 14.4 nm). The structural, vibrational, optical, and morphological properties were studied using X-ray diffraction, Raman spectroscopy, UV–Visible spectroscopy, and scanning electron microscope (SEM). A comparison of the previous and present work on the effects of irradiation on CZTS is shown in Table 1.

2 Materials and methods

One step microwave-assisted synthesis method was used to synthesize the material as mentioned in the previous reports [23, 24] with a slight modification that instead of cyclic microwave irradiation, single step microwave irradiation was carried out. In a typical synthesis process, all the required precursors were taken in an appropriate concentration and exposed to microwaves for 10 min. After that the precipitate was washed with ethanol, centrifuged and dried to get the final CZTS nanopowder. Indigenously developed Race-Track Microtron accelerator having 6 MeV energy electron beam with faraday cup attached to a counter (1 count = 10^{11} electrons) was used [25] for irradiation. X-ray diffractometer D8 Advance BRUKER AXS was used to determine crystal structure and crystallite size of

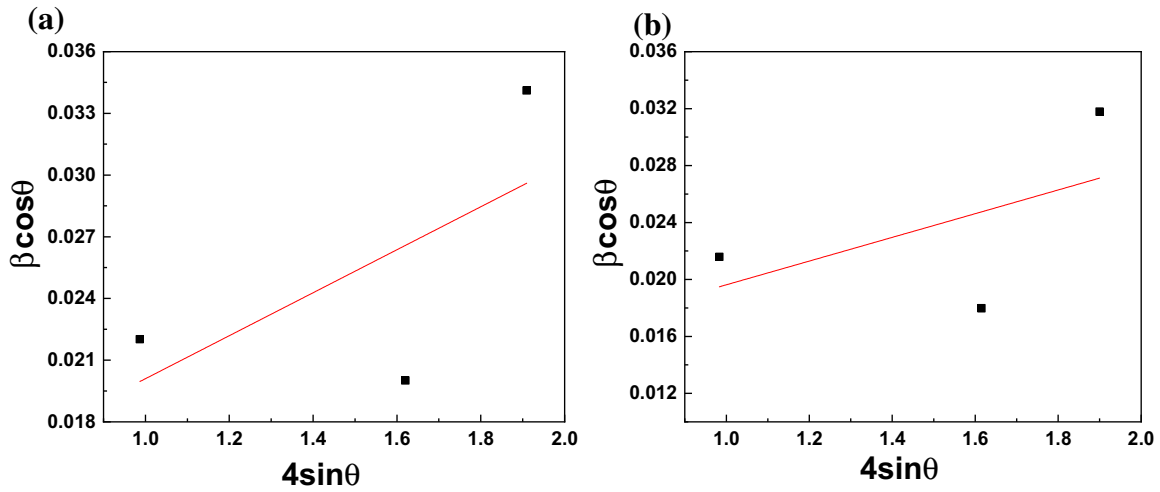

Fig. 2 Williamson-Hall Plot of **a** pristine Cu_2ZnSnS_4 and **b** Cu_2ZnSnS_4 sample irradiated with 6 MeV electronat 3 × 10^{15} e^-/cm^2 fluence

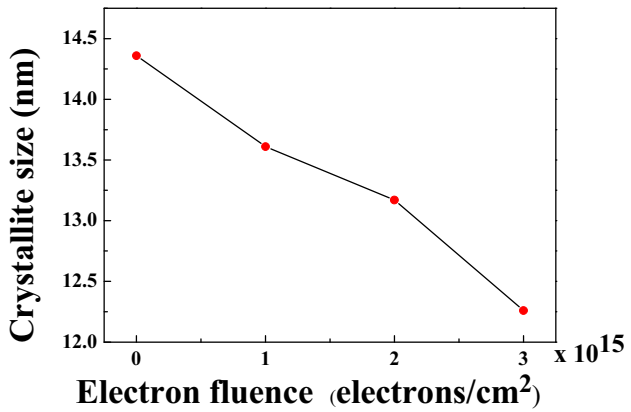

Fig. 3 Estimated crystallite size of Cu_2ZnSnS_4 samples using XRD at different irradiation fluences

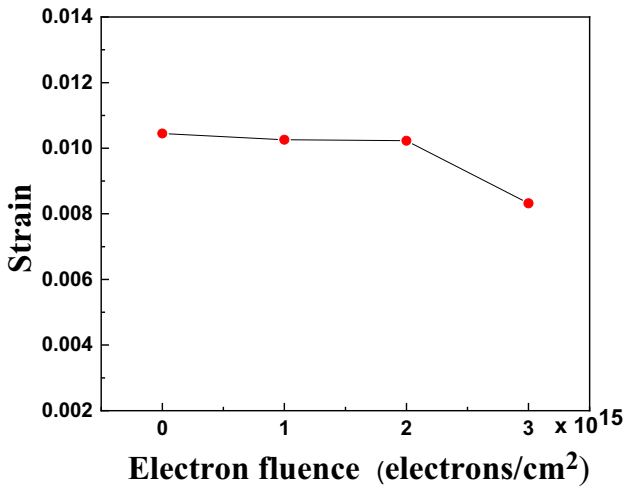

Fig. 4 Strain on Cu_2ZnSnS_4 samples calculated using XRD patterns at different irradiation fluences

the sample with Cu Kα ray of wavelength 1.54 Å. JASCO V 670, UV–Visible spectrometer was used for optical absorption measurements. For simplicity throughout the text, we are representing pristine CZTS (without irradiation) sample as A1 and 6 MeV electron irradiated with fluence 1 × 10^{15} e^-/cm^2, 2 × 10^{15} e^-/cm^2, 3 × 10^{15} e^-/cm^2 and 4 × 10^{15} e^-/cm^2 as A2, A3, A4 and A5, respectively.

Laboratory based X-Ray Diffractometer is not sufficient to differentiate the two forms of CZTS crystal structures [26, 27]. To identify various impurity phases, quantifying disorder and also to estimate the quality of crystallinity in this class of compounds Raman spectroscopy is particularly used. Renishaw Raman spectrometer was used in backscattering configuration at the excitation wavelength of 532 nm for Raman spectroscopy measurements. For Raman spectra analysis, Lorentzian function was used to fit Raman spectra to determine mode frequencies, area under the curve, FWHM and integrated intensity. Fitting was carried out with the minimum number of peaks which provides peak position, FWHM and integrated intensity. The same standard procedure is followed for the data for all electron irradiated samples.

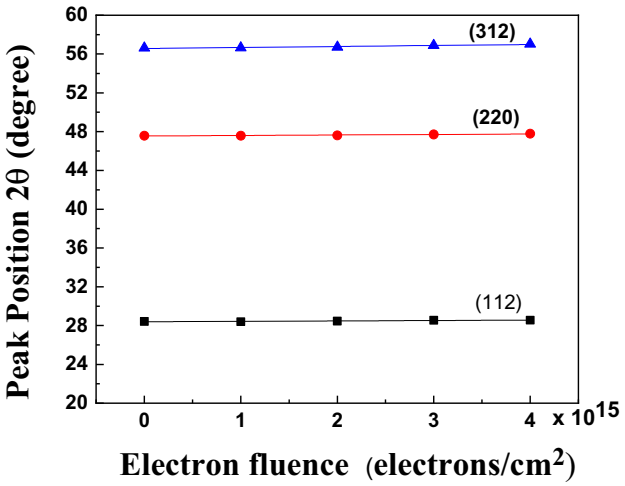

Fig. 5 Dependence of X-ray diffraction peak positions of Cu_2ZnSnS_4 samples for different electron irradiation fluences

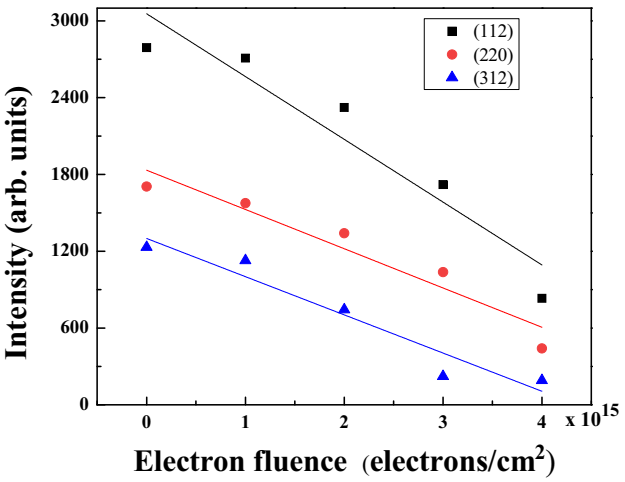

Fig. 6 Dependence of intensity (area under the curve) of (112), (220) and (312) peaks of X-ray diffraction patterns of CZTS samples for different electron irradiation fluences

3 Results and discussion

Figure 1 shows X-ray diffraction pattern of pristine nano-Cu_2ZnSnS_4 (A1) and nano-Cu_2ZnSnS_4 irradiated at different electron fluences 1×10^{15} e^-/cm^2 (A2), 2×10^{15} e^-/cm^2 (A3), 3×10^{15} e^-/cm^2 (A4) and 4×10^{15} e^-/cm^2 (A5). The broad peaks occurring at 28.4°, 47.6° and 56.5° are indexed to (112), (220) and (312) planes which are signature peaks of kesterite phase CZTS and are very well matched with JCPDS card no. 26-0575. The X-ray diffraction (XRD) pattern does not show any extra peak in pristine nano-Cu_2ZnSnS_4 which in general suggests the absence of impurity phases. Further, it is observed

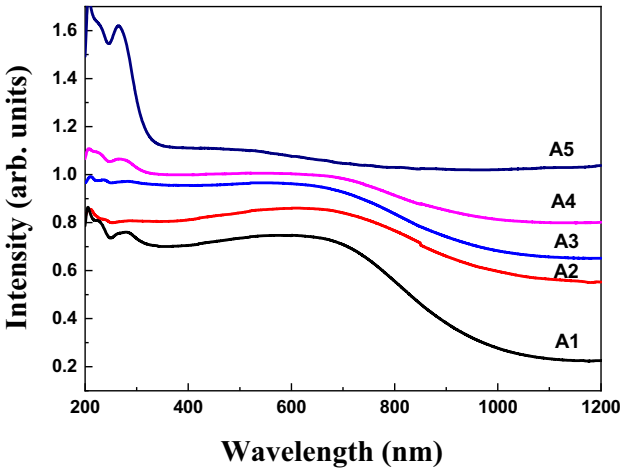

Fig. 7 UV absorption spectra of Cu_2ZnSnS_4 samples irradiated with 6 MeV electron at different fluencies

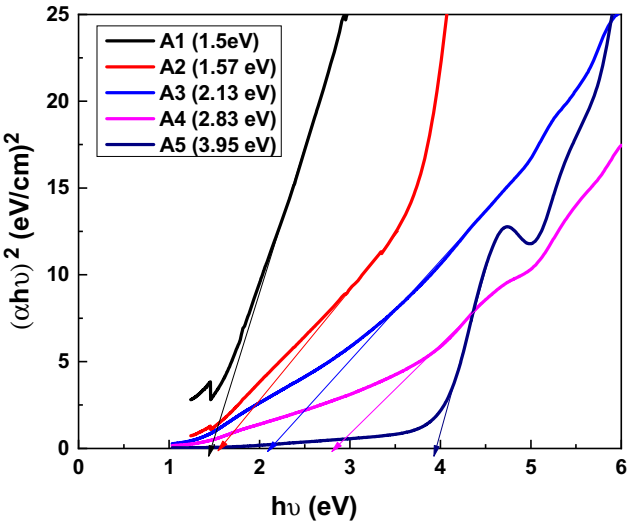

Fig. 8 Tauc plot of Cu_2ZnSnS_4 samples irradiated with 6 MeV electron at different fluences. Estimated band gaps are shown in brackets

after irradiation, there is a decrease in the peak intensities revealing that the crystallinity is decreasing with increase in electron fluence. Moreover, we can clearly observe that up to fluence of 3×10^{15} e^-/cm^2 the XRD pattern remains same, but at a fluence of 4×10^{15} e^-/cm^2 the intensity of peak at 56.5° for (312) plane completely vanished and new peaks appear at 57.9° and 62.9°. The new peaks may be attributed to the secondary phase formation or disorder arising due to the effect of electron irradiation. An important observation is that the sample did not amorphize up to the highest fluence applied. This indicates radiation stability of CZTS and is significant

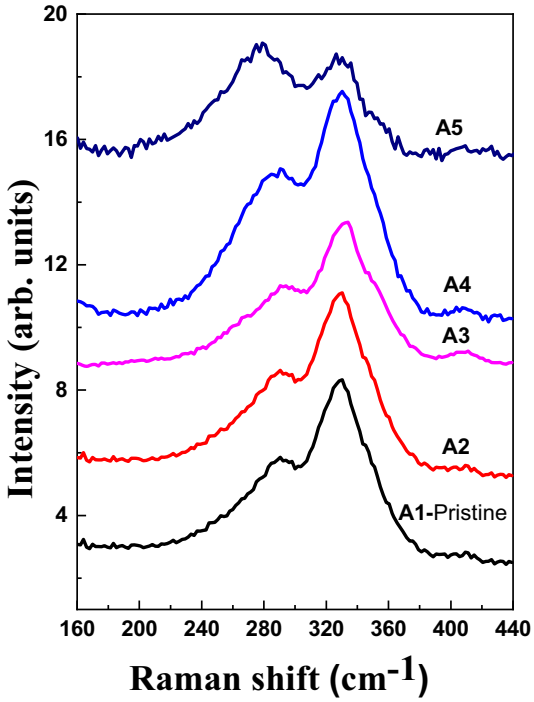

Fig. 9 Raman spectra of Cu_2ZnSnS_4 samples irradiated with 6 MeV electron at different fluences

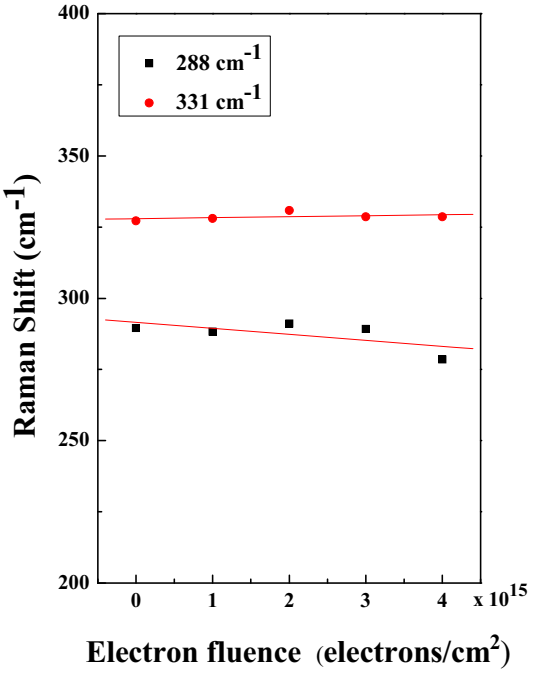

Fig. 10 Electron irradiation fluence dependence of Raman mode frequencies of CZTS samples

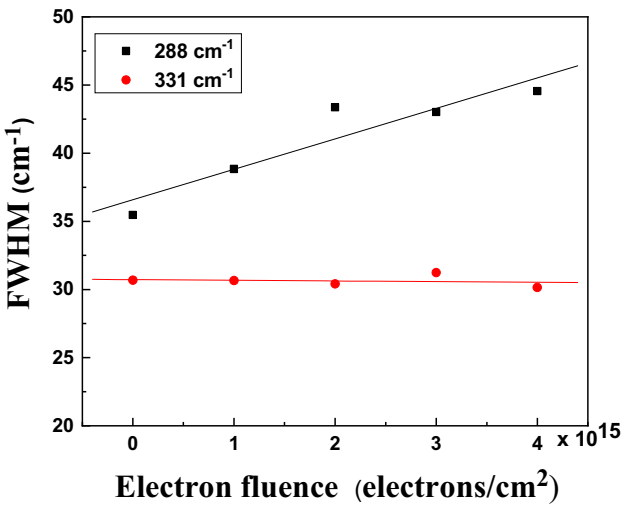

Fig. 11 Dependence of FWHM of Raman modes of nano-CZTS on electron irradiation fluence

in the context of its application as a solar cell material in space. Voigt function was used to fit X-ray diffraction patterns. To calculate crystallite size and strain on Cu_2ZnSnS_4, we have used Williamson–Hall method. Total peak broadening β_T is caused by crystallite size broadening β_D and micro-strain broadening β_ε of the crystallite.

$$\beta_T = \beta_D + \beta_\varepsilon \tag{1}$$

From Scherrer equation we know that

$$\beta_D = \frac{K\lambda}{D\cos\theta} \tag{2}$$

where θ is the diffraction angle, λ is the wavelength of X-ray (1.54 Å), D is the crystallite size and K (0.9) is shape factor.

Similarly, the X-ray diffraction peak broadening due to strain is given by:

$$\beta_\varepsilon = 4\varepsilon\tan\theta \tag{3}$$

where β_ε is the broadening due to strain, ε is the micro strain and θ is the diffraction angle.

Putting Eqs. (2) and (3) in (1) we get,

$$\beta_T = \frac{K\lambda}{D\cos\theta} + 4\varepsilon\tan\theta \tag{4}$$

Rearranging above equation, we get

$$\beta_T\cos\theta = \frac{K\lambda}{D} + 4\varepsilon\sin\theta \tag{5}$$

Equation 5 represents uniform deformation model (UDM) where it was predicted strain is uniform in all crystallographic directions [28]. $\beta_T\cos\theta$ is plotted as a function of $4\sin\theta$ for peaks of CZTS. Strain (ε) is estimated from slope of the fit and crystallite size D is estimated from the Y intercept of the fit.

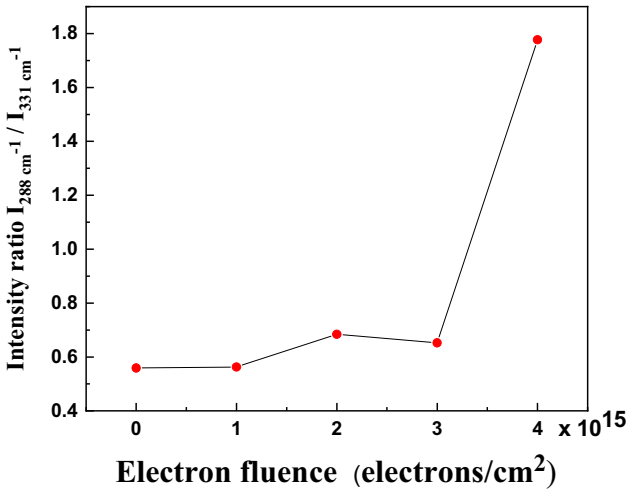

Fig. 12 Intensity ratio $I_{288\ cm-1}/I_{331\ cm-1}$ as a function of electron irradiation fluence

Figure 2 represents Williamson–Hall plot of (a) pristine CZTS and (b) CZTS sample irradiated with 6 MeV electron at 3×10^{15} e^-/cm^2 electron fluence. The crystallite size of pristine CZTS is estimated to be 14.4 nm and upon irradiation the average crystallite sizes of A2, A3 and A4 samples are obtained to be around 13.6 nm, 13.2 nm and 12.3 nm which is also represented in Fig. 3. Here we can clearly see crystallite size decreases with electron fluence. Figure 4 shows strain due to electron irradiation on of CZTS. We can clearly see that change in strain on CZTS with electron irradiation is marginal. Figure 1b shows the data for sample A5. This corresponds to 4×10^{15} e^-/cm^2 electron fluence, i.e. the highest electron irradiation; the decrease in crystallinity and formation of new phases is apparent. Estimating the peak broadening for the three peaks of interest is not unambiguous. Hence, only four points of data were employed for Figs. 3 and 4. Figure 5 shows peak position as a function of electron fluence which clearly indicates there is no change in peak position due to electron fluence, whereas area under the curve (integrated intensity) is decreasing for (112), (220) and (312) planes with increase in electron fluence. Considering pristine sample intensity as 100% for (112) peak intensity decreases to $\sim$ 30%, for (220) peak intensity decreases to $\sim$ 26% and for (312) it decreases to $\sim$ 16% for the 4×10^{15} e^-/cm^2 electron fluence as shown in Fig. 6, indicating decrease in crystallinity as decrease in XRD peak intensity generally implies decrease in crystallinity [29]. Figure 7 shows UV absorption spectra of pristine- and electron-irradiated samples of CZTS and the corresponding Tauc's plot is shown in Fig. 8. The band gap energy was calculated from the absorption spectra by extrapolating the linear portion of the graph of $(\alpha h\nu)^{1/2}$ as a function of $(h\nu)$ to the energy axis using Tauc's relation. The band gap of pristine sample, i.e. A1 is 1.5 eV and for A2, A3, A4 and A5 band gap goes on increasing to 1.57 eV, 2.13 eV, 2.83 and 3.95 eV. Therefore, with increase in electron fluence, the band gap goes on increasing. This increase in band gap may be attributed to the spatial confinement effect. The excitation of a negatively charged electron from the valence band and the resultant positively charged hole in the valence band, give rise to an exciton (electrostatically bound electron–hole pair). The exciton has a finite size within the crystal defined by the Bohr exciton diameter (a_B), which can vary from 1 to more than 100 nm depending on the material. If the size of a semiconductor nanocrystal is smaller than the size of the exciton, the charge carriers become spatially confined, which raises their energy. Therefore, the energy difference between the filled states and the empty states increases, i.e. the band gap of the semiconductor widens [30].

Figure 9 shows Raman spectra of CZTS for pristine and irradiated samples. Bands at 280 cm^{-1} and 331 cm^{-1} are the signature peaks of nano-CZTS [31–33]. From Fig. 9, we can clearly observe that up to 2×10^{15} e^-/cm^2 Raman mode frequencies of CZTS are stable, while for further irradiation at 4×10^{15} e^-/cm^2 the relative intensity of band at 280 cm^{-1}increases as compared to 331 cm^{-1} mode. Our earlier high temperature study on nano-CZTS indicated that beyond 550 K there is a considerable variation in relative intensities of 280 cm^{-1} mode and 331 cm^{-1} Raman mode frequencies, indicating phase transition from ordered kesterite to disordered kesterite structure [34]. The transition that occurs at higher irradiation dose is exactly same as transition at high temperature. Figure 10 shows electron fluence dependence of Raman mode frequencies of nano-CZTS. Here, we see that Raman mode at 331 cm^{-1} is stable with increase in electron fluence, while Raman mode frequency of the 280 cm^{-1} mode decreases marginally with electron fluence. Electron irradiation-dependent FWHM of Raman mode frequencies of nano-CZTS is plotted in Fig. 11. It shows that the width of mode at 280 cm^{-1} increases with electron fluence, but width of 331 cm^{-1} is stable which shows

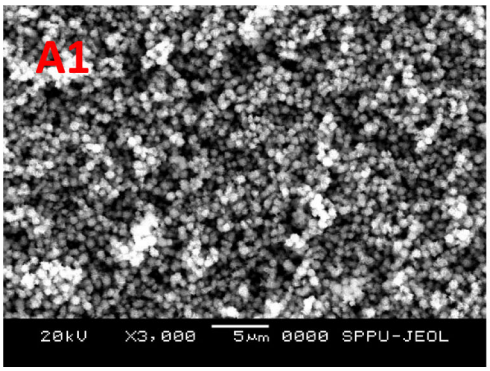
A1
20kV X3,000 5μm 0000 SPPU-JEOL

(a)

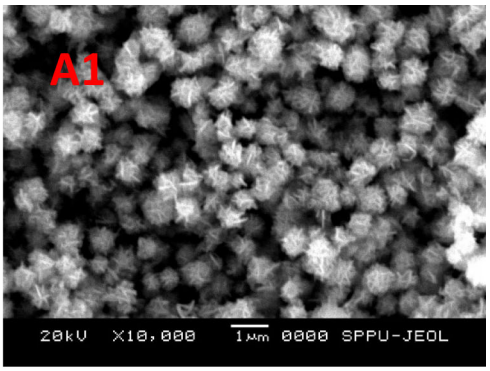
A1
20kV X10,000 1μm 0000 SPPU-JEOL

(b)

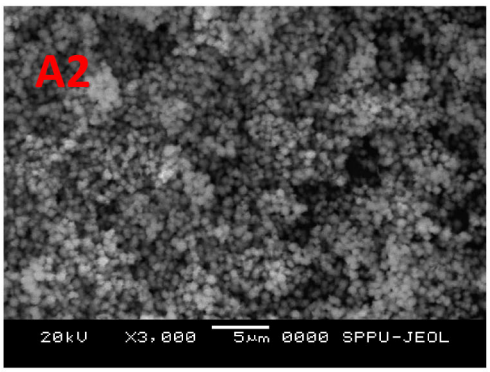
A2
20kV X3,000 5μm 0000 SPPU-JEOL

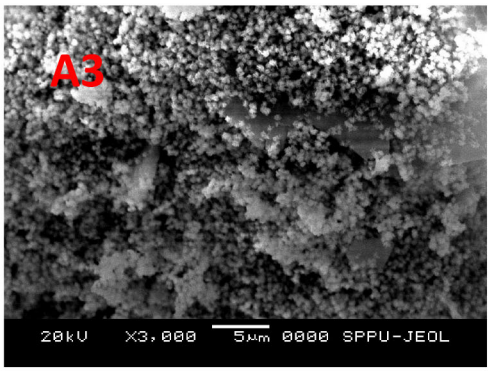
A3
20kV X3,000 5μm 0000 SPPU-JEOL

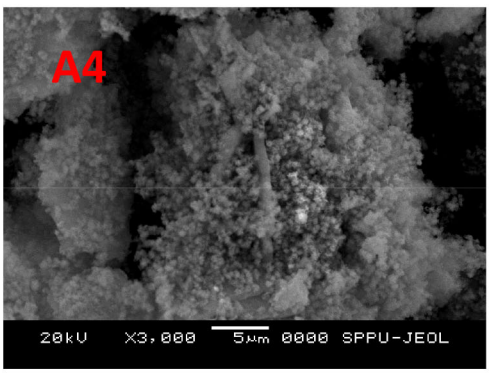
A4
20kV X3,000 5μm 0000 SPPU-JEOL

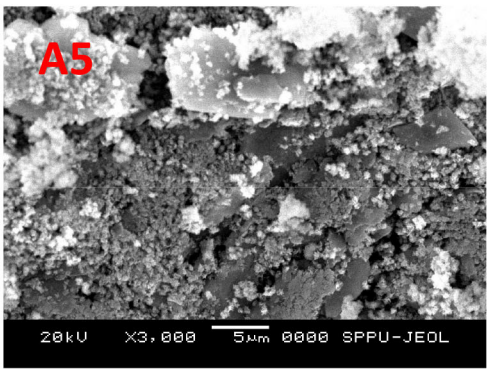
A5
20kV X3,000 5μm 0000 SPPU-JEOL

(c)

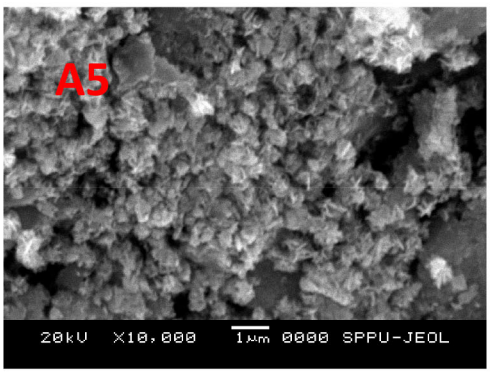
A5
20kV X10,000 1μm 0000 SPPU-JEOL

(d)

◀**Fig. 13** **a** SEM image of pristine (A1) Cu_2ZnSnS_4. **b** Pristine (A1) Cu_2ZnSnS_4 at magnified view. **c** SEM image of Cu_2ZnSnS_4 samples irradiated with 6 MeV electron at 1×10^{15} electrons/cm^2 (A2), 2×10^{15} electrons/cm^2 (A3), 3×10^{15} electrons/cm^2 (A4) and 4×10^{15} electrons/cm^2 (A5). **d** SEM image of Cu_2ZnSnS_4 after irradiation 4×10^{15} electrons/cm^2 (for 1 μm scale)

irrespective of the electron fluence the strongest mode of CZTS is stable. Intensity ratio of mode at 280 cm^{-1} to mode at 331 cm^{-1}is plotted in Fig. 12, which shows a clear increase beyond 4×10^{15} e$^-$/cm^2, indicating a phase transition to a disordered kesterite phase.

The SEM images of CZTS before irradiation are shown in Fig. 13a; it consists of hierarchical flower-like morphology having around 1 μm particle size clearly visible in magnified image Fig. 13b, c shows SEM images after different irradiation. We can clearly see for 1×10^{15} e$^-$/cm^2 there is no change in morphology but beyond this, particles start agglomerating and become irregular. For 4×10^{15} e$^-$/cm^2 irradiation fluence, the morphology is completely changed as shown in SEM image in Fig. 13d.

4 Conclusions

In conclusion, the effect of electron irradiation on $Cu_2ZnSnS_4$was investigated, to explore its radiation stability. The samples were characterized for their structural, optical, vibrational, and morphological properties using X-ray diffraction, UV–Visible spectroscopy, Raman spectroscopy, and SEM. The results reveal phase transition from ordered kesterite to disordered kesterite for 4×10^{15} e$^-$/cm^2 irradiation fluence. The XRD shows decrease in crystallite size from 14.4 to 12.3 nm with increase in electron irradiation. Also, crystallinity decreases with increase in electron irradiation. Band gap of the material changed from 1.5 to3.95 eV. Raman spectroscopic measurements confirm the structural phase transition beyond 3×10^{15} e$^-$/cm^2. SEM study reveals the morphology of hierarchical flower Cu_2ZnSnS_4 start agglomerating with electron irradiation and it completely changes at 4×10^{15} e$^-$/cm^2. The samples did not amorphize in the fluence range used and thus indicate radiation stability.

Acknowledgements

The authors are thankful to Bhabha Atomic Research Centre–Savitribai Phule Pune University Memorandum of Understanding (B.A.R.C.-S.P.P.U. MoU), University Grant Commission start-up grant for financial support to carry out this work.

References

1. T.V. Torchynska, G. Polupan, Superficies y Vacío **17**(3), 21–25 (2004)
2. M. Alurralde, M.J.L. Tamasi, C.J. Bruno, M.G. Martinez Bogado, J. Pla, J. Fernandez Vazquez, J. Duran, J. Schuff, A.A. Burlon, P. Stoliar, A.J. Kreiner, Sol. Energy Mater. Sol. Cells **82**, 531–542 (2004)
3. M. Taguchi, K. Kawamoto, S. Tsuge, T. Baba, H. Sakata, M. Morizane, K. Uchihashi, N. Nakamura, S. Kiyama, O. Oota, Prog. Photovolt. Res. Appl. **8**, 503–513 (2000)
4. N. Nagai, M. Sumitomo, M. Imaizumi, R. Fukasawa, Semicond. Sci. Technol. **21**, 201–209 (2006)
5. M. Yamaguchi, A. Khan, S.J. Taylor, M. Imaizumi, T. Hisamatsu, S. Matsuda, IEEE Trans. Electron Devices **46**, 2133–2138 (1999)
6. F. Dimroth, S. Kurtz, MRS Bull. **32**, 230–235 (2007)
7. M. Yamaguchi, Sol. Energy Mater. Sol. Cells **75**, 261–269 (2003)
8. T. Sumita, M. Imaizumi, S. Matsuda, T. Ohshima, A. Ohi, H. Itoh, Nucl. Instrum. Methods. Phys. Res. Sect. B **206**, 448–451 (2003)
9. A.W. Bett, F. Dimroth, W. Guter, R. Hoheisel, E. Oliva, S.P. Philipps, J. Schöne, G. Siefer, M. Steiner, A. Wekkeli, E. Welser, M. Meusel, W. Köstler, G. Strobl, 24th European Photovoltaic Solar Energy Conference, 21–25 (2009). https://doi.org/10.4229/24thEUPVSEC2009-1AP.1.1
10. S.-I. Sato, T. Ohshima, M. Imaizumi, J. Appl. Phys. **105**, 044504 (2009)
11. M. Yamaguchi, Sol. Energy Mater. Sol. Cells **68**, 31–53 (2001)
12. M. Ochoa, E. Yaccuzzi, P. Espinet-González, M. Barrera, E. Barrigón, M.L. Ibarra, Y. Contreras, J. García, E. López, M. Alurralde, C. Algora, E. Godfrin, I. Rey-Stolle, J. Plá, Sol. Energy Mater. Sol. Cells. **159**, 576–582 (2017)
13. J.G.J. Adams, V.C. Elarde, G. Hillier, C. Stender, F. Tuminello, A. Wibowo, C. Youtsey, Z. Bittner, S.M. Hubbard, E.B. Clark, M.F. Piszczor, M. Osowski, IEEE 39th Photovoltaic Specialists Conference (PVSC), IEEE, 3229–3232 (2013). https://doi.org/10.1109/PVSC.2013.6745140

14. J. Kuendiga, M. Goetza, A. Shaha, L. Gerlachb, E. Fernandez, Sol. Energy Mater. Sol. Cells **79**, 425–438 (2003)
15. M.R. Reddy, Sol. Energy Mater. Sol. Cells. **77**, 175–208 (2003)
16. A. Hamache, N. Sengouga, A. Meftah, M. Henini, Radiat. Phys. Chem. **123**, 103–108 (2016)
17. A. Jasenek, U. Rau, K. Weinert, I.M. Kotschau, G. Hanna, G. Voorwinden, M. Powalla, H.W. Schock, J.H. Werner, Thin Solid Films **387**, 228–230 (2001)
18. K. Otte, L. Makhova, A. Braun, I. Konovalov, Thin Solid Films **511**, 613–622 (2006)
19. M. Sauli, C. Nefzi, Z. Seboui, A. Mejri, R. Vidu, N. Kamoun-Turki, Mater. Sci. Semicond. Process. **83**, 50–57 (2018)
20. M. Sugiyama, S. Aihara, Y. Shimamune, H. Katagiri, Thin Solid Films **642**, 311–315 (2017)
21. S.S. Suvanam, J. Larsen, N. Ross, V. Kosyak, A. Hallén, C.P. Björkman, Sol. Energy Mater. Sol. Cells **185**, 16 (2018)
22. W.M. Parkin, A. Balan, L. Liang, P.M. Das, M. Lamparski, C.H. Naylor, J.A. Rodríguez-Manzo, A.T. Charlie Johnson, V. Meunier, M. Drndić, ACS Nano **10**(4), 4134–4142 (2016)
23. S.P. Kandare, S.D. Dhole, V.N. Bhoraskar, S.S. Dahiwale, AIP Conf. Proc. **1731**, 050084 (2016)
24. S.P. Kandare, A.B. Thorat, S.D. Dhole, S.S. Dahiwale, Ind. J. Pure Appl. Phys. **57**, 7–13 (2019). http://nopr.niscair.res.in/handle/123456789/45633
25. V.B. Asgekar, R.K. Bhalla, B.S. Raye, M.R. Bhiday, V.N. Bhoraskar, Pramana **15**(5), 479–493 (1980)
26. M. Dimitrievska, F. Boero, A.P. Litvinchuk, S. Delsante, G. Borzone, A.P. Rodriguez, V. I-Roca, Inorg. Chem. **56**(6), 3467–3474 (2017)
27. M. Dimitrievska, A. Fairbrother, X. Fontane, T. Jawhari, V. I-Roca, E. Saucedo, A. Perez-Rodriguez, App. Phys. Lett. **104**, 021901 (2014)
28. Y.T. Prabhu, K.V. Rao, V.S. Sai Kumar, B.S. Kumari, World J. Nano Sci. Eng. **4**, 21–28 (2014)
29. D.S. Rana, D.K. Chaturvedi, J.K. Quamara, J. Mater. Eng. Perform. **20**, 276–282 (2011)
30. A.M. Smith, S. Nie, Acc. Chem. Res. **43**, 190 (2010)
31. J. Park, M. Song, W.M. Jung, W. Young Lee, H. Kim, Y. Kim, C. Hwang, I.W. Shim, Dalton Trans. **42**, 10545 (2013)
32. M. Dimitrievska, A. Fairbrother, A. Perez-Rodrıguez, E. Saucedo, V. Izquierdo-Roca, Acta Mater. **70**, 272–280 (2014)
33. Y. Zhao, W. Tao, X. Chen, J. Liu, A. Wei, J. Mater. Sci. Mater. Electron **26**, 5645 (2015)
34. S.P. Kandare, S.S. Dahiwale, S.D. Dhole, M.N. Rao, R. Rao, Mater. Sci. Semicond. Process. **102**, 104594 (2019)